



ELSEVIER

Available online at www.sciencedirect.com

ScienceDirect

journal homepage: www.elsevier.com/locate/ijhe

Two-dimensional molybdenum disulfide and tungsten disulfide interleaved nanowalls constructed on silk cocoon-derived N-doped carbon fibers for hydrogen evolution reaction

QingFa Wang^{a,*,**}, RuoPing Yanzhang^a, XiaoNa Ren^a, Han Zhu^{b,*},
Ming Zhang^b, MingLiang Du^b

^a Key Laboratory for Green Chemical Technology of the Ministry of Education, School of Chemical Engineering and Technology, Tianjin University, 92 Weijin Road, Tianjin, 300072, PR China

^b Department of Materials Engineering, College of Materials and Textiles, Zhejiang Sci-Tech University, Hangzhou, 310018, PR China

ARTICLE INFO

Article history:

Received 14 June 2016

Received in revised form

23 July 2016

Accepted 28 July 2016

Available online xxx

Keywords:

Silk derived N-doped carbon

Molybdenum sulfides

Tungsten disulfide

Hydrogen evolution reaction

Electrocatalysts

ABSTRACT

Finding cost-effective, active and durable catalyst materials for energy applications, such as electrocatalytic hydrogen production, is an intriguing challenge. Here, a facile and effective approach to the design and construction of two-dimensional MoS₂ and WS₂ interleaved nanowalls with maximum exposures of active edges on silk-derived N-doped carbon fibers (SNCF) was demonstrated. The morphological evolutions of the MoS₂ and WS₂ nanocrystals on the SNCF from crescent-like nanosheets to an interleaved nanowall network can be obtained by adjusting the concentrations of the Mo and W precursors. These robust MoS₂/SNCF and WS₂/SNCF electrocatalysts exhibit prominent hydrogen evolution reaction (HER) activities with onset potentials of −40 and −96 mV and Tafel slopes of 60 and 66 mV dec^{−1}, respectively. The overpotentials (η) at $j = -10 \text{ mA cm}^{-2}$ for MoS₂/SNCF and WS₂/SNCF are −102 and −157 mV, respectively. In addition, MoS₂/SNCF and WS₂/SNCF are both able to sustain continuous HER operation for 10 h under working conditions with only a slight degradation in current densities, implying excellent durability and a prospect for practical applications.

© 2016 Hydrogen Energy Publications LLC. Published by Elsevier Ltd. All rights reserved.

Introduction

Hydrogen is a clean and sustainable energy carrier that provides an environmentally friendly alternative energy source to meet future global energy demands [1]. The production of

hydrogen by electrocatalytic or solar-driven water splitting requires highly efficient and robust catalyst materials [1,2]. The platinum group is at present the most active catalysts for the hydrogen evolution reaction (HER). Unfortunately, the high cost and low elemental abundance of the platinum group metals limit their application in large-scale hydrogen

* Corresponding author. Fax: +86 571 86843255.

** Corresponding author. Fax: +86 22 27892340.

E-mail addresses: qfwang@tju.edu.cn (Q. Wang), zhuhanfj@zstu.edu.cn (H. Zhu).

<http://dx.doi.org/10.1016/j.ijhydene.2016.07.257>

0360-3199/© 2016 Hydrogen Energy Publications LLC. Published by Elsevier Ltd. All rights reserved.

production [3,4]. Motivated by this challenge, the search for cost-effective, Earth-abundant materials with both high HER activity at low overpotentials and excellent stability has recently attracted significant research interest and has become an important pursuit toward enabling a hydrogen economy [5,6].

Various classes of Earth-abundant transition metal compounds, such as MoS₂ [7], WS₂ [8], CoS₂ [1], CoSe₂ [9], and MoP [10] have been recently identified as promising HER electrocatalysts. Two-dimensional MoS₂ or WS₂ have been considered as the most promising catalysts because their hydrogen binding energies are comparable to that of the Pt-group metals, as determined by density functional theory calculations [7,8]. From both theoretical calculations and experimental studies, it is known that the HER active sites arise from the edges rather than the basal plane of an MoS₂ sheet [7,8]. Therefore, to realize the ideal catalytic activity of MoS₂, we should find an effective approach to design and construct novel structures of MoS₂ with exposed active edges. In addition, the poor conductivity of semiconducting MoS₂ limits the electron transfer and the electrocatalytic efficiency for the HER.

Carbon materials, such as graphene [11], carbon nanotubes [12], porous carbon [13] and carbon nanofibers [14], have been widely used to improve the electrochemical performance of catalysts. Recently, our group has reported that carbon materials not only serve as substrates but can also confine the growth of MoS₂ or WS₂, leading to novel nanostructures of two-dimensional transition metal sulfides with abundant active sites and high electrocatalytic activity toward the HER [15–17]. Carbon materials derived from natural resources and their conversion into functional building units are highly desirable [18,19]. Silk fiber is a filamentous natural protein fiber made of repeated amino acid patterns [20]. Researches on silk fibers are generally focused on its applications in the biomedical and clinical fields because of its excellent biocompatibility and biodegradability [21–23]. Moreover, silk fibers have a wealth of polypeptides and a high content of C, N, and O elements [21–25], which might provide a great opportunity for conversion into naturally derived heteroatom-doped carbon catalysts.

Herein, we utilized the chemical composition and fibrous structure of silk fibers to produce N-doped carbon fibers through simple pyrolysis. The resulting silk-derived N-doped carbon fibers (SNCF) serve as an effective substrate for the design and construction of MoS₂ and WS₂ nanowalls with exposed active-edges. The morphological evolution of MoS₂ and WS₂ nanocrystals on the SNCF from crescent-like nanosheets to an interleaved nanowall network can be obtained by adjusting the concentrations of the Mo and W precursors. The HER performances of various catalysts were measured to confirm the realization of the active-edge control, and a comprehensive investigation of the growth mechanisms was provided. The present investigation aimed to determine whether nanowalls with vertically aligned and densely packed MoS₂ and WS₂ nanosheets on SNCF possess the most exposed active edges and obtained outstanding HER performance. The robust MoS₂/SNCF and WS₂/SNCF electrocatalysts exhibit preeminent HER activity with onset potentials of –40 and –96 mV and Tafel slopes of 60 and 66 mV dec^{–1},

respectively. The overpotentials (η) at $j = -10 \text{ mA cm}^{-2}$ (mV) for MoS₂/SNCF and WS₂/SNCF are –102 and –157 mV, respectively. In addition, MoS₂/SNCF and WS₂/SNCF are both able to sustain continuous HER operation for 10 h under working conditions with only a slight degradation in the current density. The results reveal a stability under HER conditions and a strong coupling of the MoS₂ and WS₂ nanowalls to the SNCF, implying excellent durability and a prospect for practical applications.

Experiment section

Materials

Silk cocoons were prepared by feeding the *Bombyx mori* in our lab. Pt/C (20 wt %) and the Nafion solution (5 wt %) were purchased from Sigma–Aldrich. (NH₄)₂MoS₄, (NH₄)₂WS₄ and dimethyl formamide (DMF, 95%) were obtained commercially from Shanghai Civi Chemical Technology Co., Ltd. All chemicals were used as received without further purification. The water used throughout all experiments was purified through a Millipore system.

Preparation of the silk-derived carbon fibers (SNCF)

Natural silk cocoons were prepared by feeding the *Bombyx mori* in our lab. In brief, the obtained silk cocoons were treated with distilled water in an ultrasonic bath for 2 h to remove adsorbed impurities. Then, the silk cocoons were dried at 50 °C for 12 h. The cleaned silk cocoons were placed into a chemical vapor deposition (CVD) furnace and carbonized at 900 °C at a heating rate of 4 °C/min for 3 h in an Ar/NH₃ atmosphere. The obtained silk-derived N-doped carbon fibers were treated with 1 M HNO₃ three times, washed with deionized water and dried at 60 °C for 24 h in a vacuum oven.

Preparation of the two-dimensional MoS₂ and WS₂ nanowall network on silk-derived carbon fibers

The as-prepared silk-derived carbon fibers served as the substrate for the growth of the two-dimensional MoS₂ and WS₂ nanosheets. Briefly, 110 mg of (NH₄)₂MoS₄ was dissolved in 50 mL of a DMF solution containing 330 mg of the as-prepared silk-derived N-doped carbon fibers. The mixture was stirred at room temperature for 2 h, transferred to a 50 mL Teflon-lined autoclave and kept in an oven at 200 °C for 12 h. Finally, the product was centrifuged, washed with distilled water, and then centrifuged repeatedly to remove the DMF. Pure MoS₂ nanoflowers were prepared using the same procedure in the absence of the SNCF. The preparation of WS₂ nanowalls were using the same procedure.

Fabrication of the catalyst-modified glassy carbon electrode (GCE)

To prepare the working electrode, 3 mg of the catalyst and 25 μL of the 5 wt % Nafion solution were dispersed in 1 mL of an isopropanol/water (3:1, v/v) mixed solvent, followed by ultrasonication for at least 30 min. Then, 5 μL of the mixture

was dropped onto the glassy carbon electrode (loading: $\sim 0.36 \text{ mg cm}^{-2}$).

Electrochemical measurements

All electrochemical tests were performed at room temperature in a standard three-electrode system controlled by an Autolab potentiostat/galvanostat (Model PGSTAT302N) workstation. A graphite rod and a saturated calomel electrode (SCE) were used as the counter and reference electrodes, respectively. Prior to the start of each experiment, the electrolyte was degassed by bubbling Ar for 30 min. The electrochemical impedance spectroscopy (EIS) measurements were carried out in the same configuration at an overpotential of $\eta = -300 \text{ mV}$ from 10^6 to 0.02 Hz with an AC voltage of 5 mV . All of the potentials reported in the present investigation were against a reversible hydrogen electrode (RHE). For the conversion of the obtained potential (vs Hg/HgO) to the RHE, the potentials were referenced to the RHE by the following summation ($0.244 + 0.059 \text{ pH}$) V for SCE.

Characterizations

The morphologies of the as-prepared samples were investigated using a JSM-2100 transmission electron microscope (JEOL, Japan) at an acceleration voltage of 200 kV . Field-emission scanning electron microscopy (FE-SEM, JEOL, Japan) was performed using a JSM-6700F at an acceleration voltage of 3 kV . High-angle annular dark-field scanning transmission electron microscopy (HAADF-STEM) images, STEM mapping, and line-scan energy dispersive X-ray spectroscopy (EDX) were recorded using a STEM (Tecnai G2 F30S-Twin, Philips-FEI) at an acceleration voltage of 300 kV . X-ray diffraction (XRD) patterns were analyzed using a Bruker AXS

D8 DISCOVER X-ray diffractometer with Cu K_α radiation ($\lambda = 1.5406 \text{ \AA}$) at a scanning rate of $0.02 \text{ 2}\theta \text{ s}^{-1}$ in a 2θ range of 10° – 80° . X-ray photoelectron spectra of the products were recorded using an X-ray photoelectron spectrometer (Kratos Axis Ultra DLD) with an Al (mono) K_α source (1486.6 eV). The Al K_α source was operated at 15 kV and 10 mA . Raman spectra were recorded using a Renishaw in via Raman microscope (LabRAM HR800) with a 532 nm laser excitation source.

Results and discussion

Silk cocoons produced by the *B. mori* silkworm are among the most abundant polymers in nature, and more than 480,000 tons per year are cultivated all over the world [26,27]. The silk fibers consist of fibrous proteins, known as fibroin, and sericin, which surrounds the fibroin fibers and cements them together. The silk cocoon consists of hundreds of individual fibers with diameters in the range of 10 – $20 \text{ }\mu\text{m}$, as shown in Fig. S1. Twin fibers with smooth surfaces are distributed randomly, forming a 3D network. After the carbonization at 900°C in an Ar/ NH_3 atmosphere, the organic silk fibers convert into carbonized fibers (CFs), as shown in Fig. 1a. There are many small pores randomly distributed across the surfaces. The average diameter of the CFs decreases to approximately $1 \text{ }\mu\text{m}$ because of the graphitization process. A high-resolution TEM image reveals that the CF surface exhibits a small porous network (inset in Fig. 1c). In addition, Fig. 1c reveals the disordered lattice fringes of carbon, demonstrating the partial crystallinity. The silk-derived carbon fibers are used as the substrate for the growth of the two-dimensional MoS_2 nanocrystals. As shown in Fig. 1b, large amounts of the MoS_2 crystals were vertically and densely grown on the surfaces of the SNCF, leading to the formation of MoS_2 nanowalls

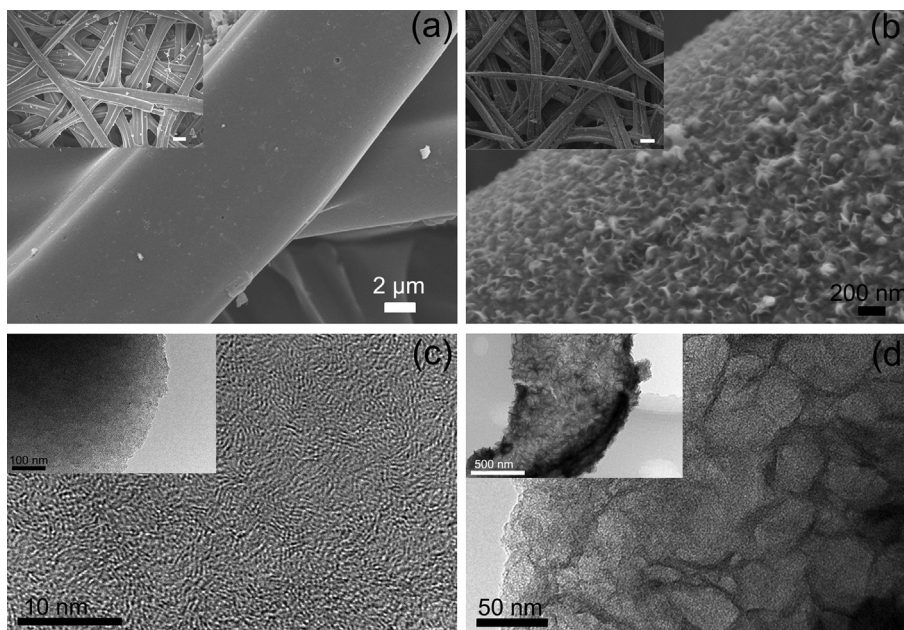


Fig. 1 – TEM images of (a) the SNCF and (b) the MoS_2/SNCF . (c) An HRTEM image of the SNCF, and the inset in (c) is the low magnification TEM image of the SNCF. (d) A high magnification TEM image of MoS_2/SNCF , and the inset in (d) is the low magnification TEM image of the MoS_2/SNCF .

throughout the SNCF. The vertical MoS₂ nanosheets interlace on the surfaces of the SNCF and form nanowalls. As shown in Fig. 1d, from the TEM images, there are many oval holes among the interlaced MoS₂ nanowalls, forming a 3D network through strong interactions. The vertical MoS₂ nanowalls on the SNCF have a maximum exposure of edges, which are the active sites for the electrocatalytic HER.

In contrast, as shown in Fig. S2, pure MoS₂ synthesized without the SNCF exhibit substantial folding and agglomeration. They resemble rosemary buds with lots of edges buried inside because this configuration is thermodynamically stable. In the presence of the SNCF, as exhibited in Fig. 1b, the MoS₂ nanosheets vertically and densely grew on the SNCF with a large amount of edges exposed. From this point of view, the SNCF substrate is significant for the achievement of the edge-rich morphology.

As shown in Fig. 2a, the MoS₂ nanowalls consist of several layers, and the holes in the nanowalls exhibit an oval morphology. The exposed edges of the MoS₂ nanowalls clearly exhibit an interlayer distance of 0.67 nm, corresponding to the (002) plane of MoS₂. In the HAADF-STEM image of MoS₂/SNCF, the interlaced MoS₂ nanowalls and the 3D network formed from strong interactions are clearly observed (Fig. 2b). The STEM image and corresponding EDX elemental mapping images of MoS₂/SNCF are shown in Fig. 2c–g. The strong and uniform signals of carbon and nitrogen correspond to the SNCF substrate, indicating the formation of an N-doped carbon nanostructure. In addition, the signals for Mo and S are well matched with the white MoS₂ morphology in Fig. 2c, confirming the successful preparation of the interlaced MoS₂ nanowalls and the 3D network.

XRD and Raman spectroscopy were carried out to further investigate the structure of the products. The SF cocoon displays a sharp main peak at 19.6°, and the peak corresponds to the (&200) diffraction peak of silk, exhibiting a typical β -sheet crystalline structure (Fig. 3) [28]. After the graphitization process, the SNCF exhibits two characteristic peaks located at approximately $2\theta = 24^\circ$ and 44° , corresponding to the (#002) and (#101) planes of the hexagonal graphite (JCPDS card no. 41-1487)

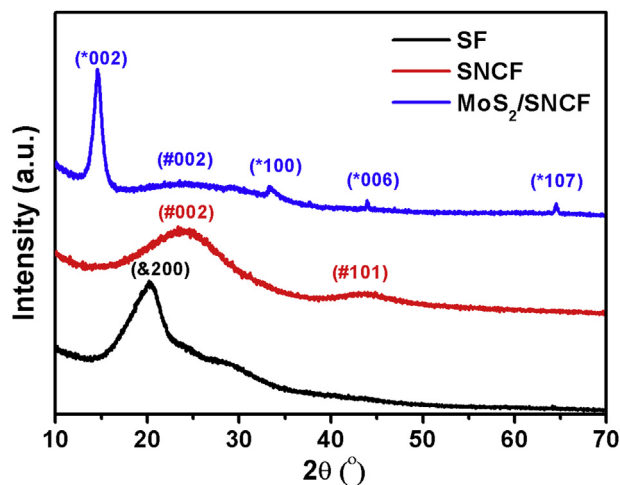


Fig. 3 – XRD patterns of the SFs, SNCF and MoS₂/SNCF hybrid.

[29]. After the growth of the interlaced MoS₂ nanowalls, the MoS₂/SNCF hybrid exhibits five diffraction peaks located at 14.7°, 24.3°, 33.3°, 44.1° and 64.5°. The sharp peak at 14.7° and the other three weak peaks at 33.3°, 44.1° and 64.5° correspond to the (*002), (*100), (*006) and (*107) planes of the hexagonal MoS₂ (2H-MoS₂, JCPDS 37-1492) [30,31]. In comparison, the XRD pattern of pure MoS₂ was shown in Fig. S3. Because of the growth of MoS₂ nanowalls on the SNCF surfaces, the (002) plane ascribed to carbon becomes weak, indicating the dense growth of the MoS₂ nanowalls. It is found that the MoS₂/SNCF exhibits an intense peak at 14.7° that is ascribed to the (002) plane of MoS₂; relatively weaker peaks are noted for the (*002), (*100), (*006) and (*107) planes. It is demonstrated that most of the MoS₂ nanosheets grew vertically on the surfaces of the SNCF and further formed the integrated MoS₂ nanowalls and 3D network, leading to a maximal exposure of the (002) planes of MoS₂.

Raman spectroscopy is an effective tool to detect the doping effect in the silk-derived carbon fiber. As shown in Fig. 4a, the Raman spectrum of the SNCF exhibits the D band

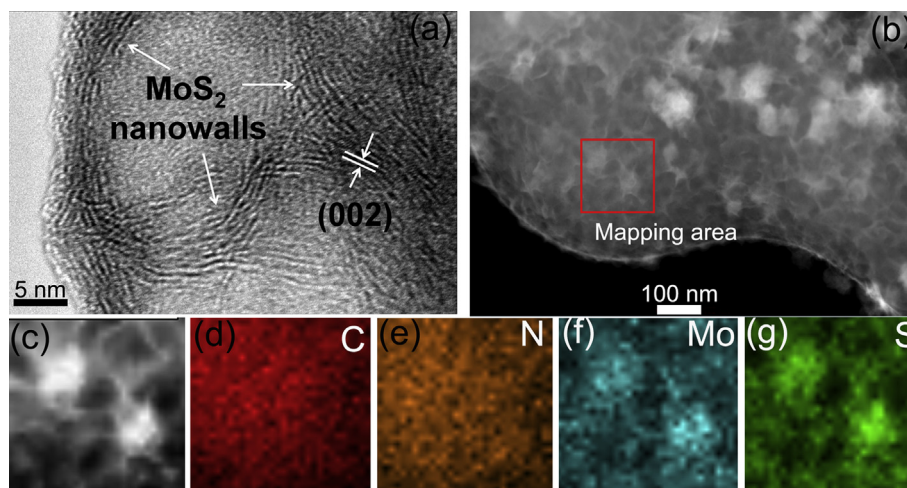


Fig. 2 – (a) HRTEM image of the MoS₂ nanowalls on SNCF. (b) HAADF-STEM image of MoS₂/SNCF. (c) HAADF-STEM and (h–k) STEM-EDS mapping images of the MoS₂ nanowalls on SNCF. The concentration of the Mo precursor was 2.2 mg mL⁻¹.

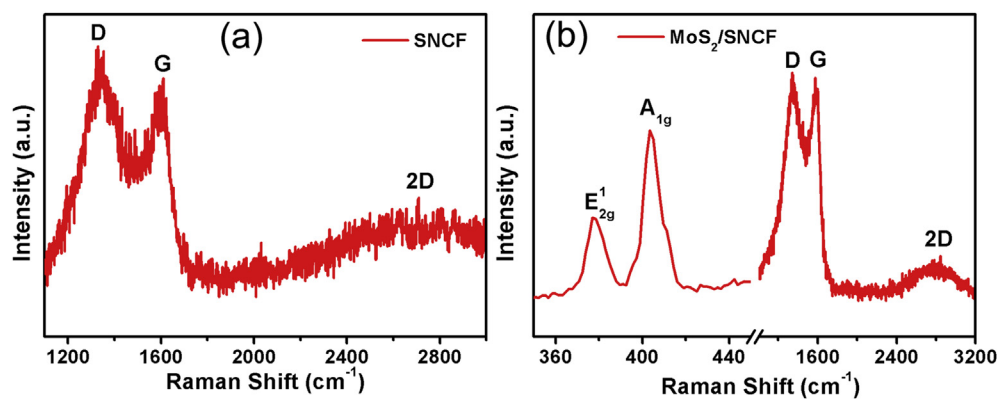


Fig. 4 – Raman spectra of the (a) SNCF and (b) MoS₂/SNCF hybrid.

at 1339 cm⁻¹, the G band at 1613 cm⁻¹ and the 2D band at 2708 cm⁻¹ [32]. The relatively high intensity of the D band for the SNCF is attributed to the introduction of nitrogen atoms into the carbon structure [32,33]. It is known that defects may include bond disorder and vacancies in the carbon lattice induced by nitrogen doping [32,33]. The Raman spectrum of MoS₂/SNCF shown in Fig. 4b confirms the formation of a pure MoS₂ phase on the SNCF. The MoS₂ nanowalls exhibit sharp peaks at 380 cm⁻¹ (E_{2g}¹) and 406 cm⁻¹ (A_{1g}¹) that are due to the first order Raman vibration modes within the S–Mo–S layer [29,30,34].

XPS measurements were further performed to elucidate the chemical structure, the atomic valence states and the composition of pure SFs and the MoS₂/SNCF hybrid. The overall XPS spectrum measured for the pure SFs exhibits signals for carbon, nitrogen, and oxygen, as shown in Fig. S4. The C 1s XPS spectrum of the pure silk cocoon was fitted by four peaks (Fig. 5a) with binding energies (BEs) at approximately 284.5, 285.2, 286.0 and 287.5 eV, which are attributed to –C–C/H, –C–N, C–OH/C–N and –O=C–N groups, respectively [35,36]. The O=C–N (287.8 eV) group reflects the carbon on the peptide backbone, while the –C–C/H (284.6 eV) group reflects the aliphatic C–C carbons of the amino acid pendant groups. The peak associated with the O=C–N group in the peptide backbone (287.6 eV) indicates that more of this peptide backbone group is associated with β-structures that are located at the surface than amorphous structures [37]. The N 1s spectrum for the silk fibers (Fig. 5b) exhibits a single main peak with a BE of 399.3 eV, corresponding to the amino acids on the silk fiber surfaces.

After the graphitization process, the C 1s spectrum of the as-prepared SNCF exhibits four peaks with BEs at 284.7, 285.5, 286.5 and 289.1 eV (Fig. 5c). The peak at 284.6 eV corresponds to graphitic C. The peak at 285.2 eV is associated with the C–N bond corresponding to the N-sp² C bonds, which may originate from the substituted N atoms and defects or the edge of the N-doped CF [38]. Because of the higher electronegativity of N atoms, the weaker peaks at 286.4 and 289.2 eV are ascribed to the C–O and O–C=O groups in the N-doped CFs, suggesting that the surfaces of the silk-derived N-doped CFs generate large amounts of N and O groups after carbonization treatment. The N and O groups on the SNCF surfaces are great nucleation points for the growth of MoS₂ nanowalls.

The N 1s spectrum (Fig. 5d) of the SNCF was deconvoluted into three peaks with BEs of 401.3, 400.3 and 398.4 eV, which are attributed to the quaternary (N-Q), the pyridinic nitrogen group (N-5) and the pyridinic nitrogen group (N-6), respectively [37–39]. These results indicate the conversion of the N atoms from the amino groups in the SFs into N-6, N-5 and N-Q during the carbonization process. It has been reported that pyridinic- and graphitic-N play important roles in the catalytic activity of the carbon catalyst because of their high charge densities [39,40]. In the present investigation, the pyridinic- and graphitic-N are the predominant species, which may enhance the electrocatalytic activity for the HER. In addition, the STEM-EDX mapping images (Fig. 2) exhibit the homogeneous distribution of nitrogen across the surface, which could be beneficial for the activity of the resulting catalyst.

The overall XPS spectrum measured for the MoS₂/SNCF hybrid exhibits signals for carbon, nitrogen, oxygen, molybdenum and sulfur, as shown in Fig. S5. The C 1s and N 1s spectra of the MoS₂/SNCF hybrid did not change, indicating that the grown MoS₂ nanowalls did not affect the composition of the SNCF, as shown in Fig. S6. The XPS C 1s spectrum of MoS₂/SNCF exhibits a single peak located at ~284.4 eV (Fig. S6), and it is attributed to graphitic carbon atoms [39,40]. The spectrum of the MoS₂/SNCF hybrid has the same shape as that of the SCNFs, implying that the chemical state of the carbon atoms was not markedly changed after MoS₂ growth (Fig. S7). However, the position of the C 1s line of the composite is downshifted by ~0.2 eV from that of the pristine SNCF (284.6 eV), indicating a charge transfer from the SNCF to the MoS₂ [34] that may improve the catalytic activity.

The high-resolution XPS of the Mo 3d region of the hybrid is shown in Fig. 5e, and it can be deconvoluted into four peaks. The distinct doublets at 332.3 and 229.4 eV correspond to the Mo 3d_{3/2} and 3d_{5/2} spin–orbit couplings, which are characteristic peaks of the MoS₂ crystal [41]. The other two peaks centered at 225.1 and 227.0 eV correspond to the S 2s binding energy of MoS₂ and that of the bridging disulfides (S₂²⁻) [41,42]. The sulfur species were determined from the high-resolution XPS S 2p spectrum, as shown in Fig. 5f. The main doublet located at binding energies of 161.2 and 162.6 eV corresponds to the S 2p_{3/2} and S 2p_{1/2} lines of MoS₂ [41–43]. Meanwhile, the peak at 163.6 eV suggests the existence of bridging disulfides (S₂²⁻) or polysulfides (S_n²⁻). The high binding energy peak at 167.2 eV is assigned to the S⁴⁺ species in the sulfate group

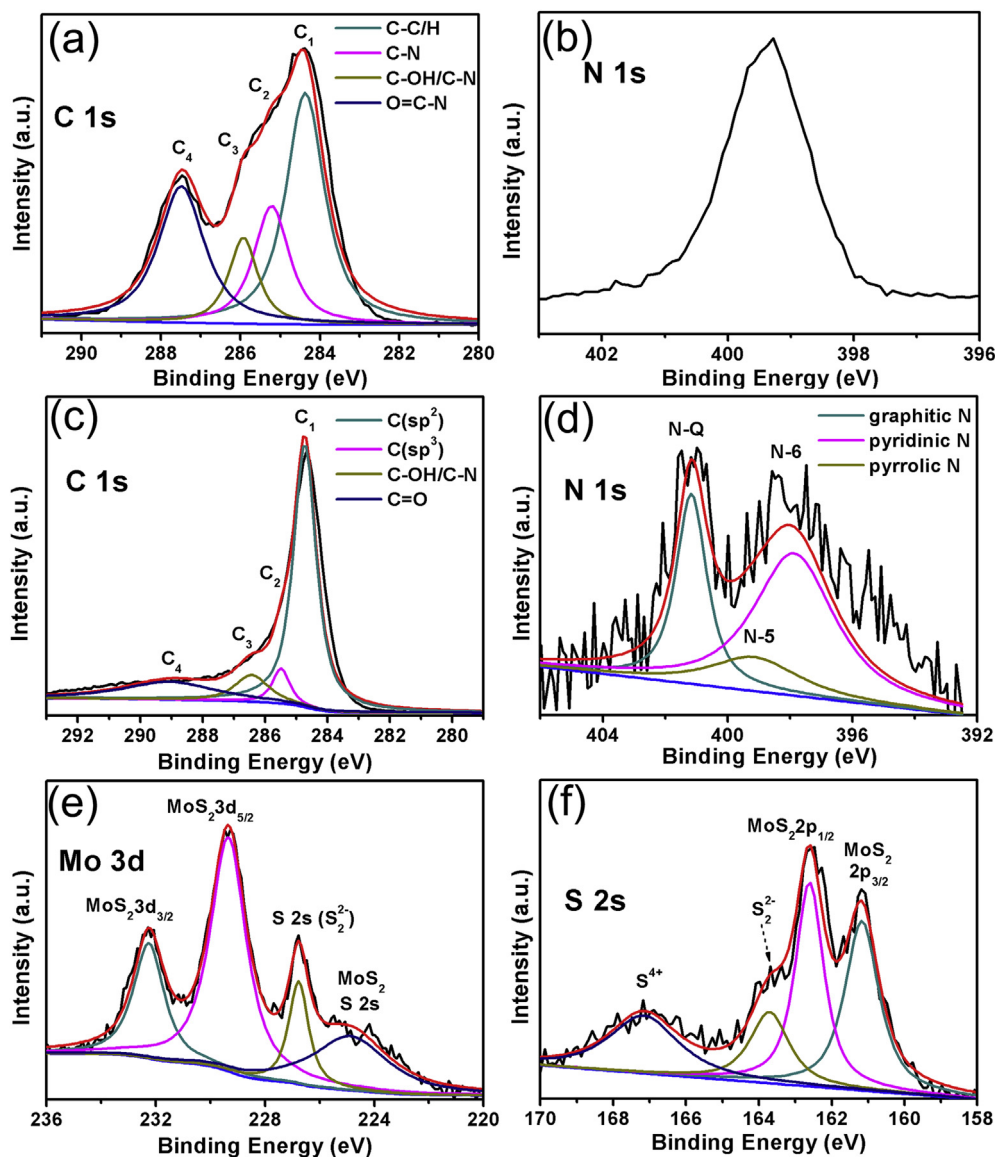


Fig. 5 – The (a) C 1s and (b) N 1s XPS spectra of SF. The (c) C 1s and (d) N 1s XPS spectra of SNCF. The (e) Mo 3d and (f) S 2s XPS spectra of the MoS₂/SNCF hybrid.

(SO₃²⁻) [41–44]. These groups could be located at the edges of the MoS₂ layers, leading to the formation of an S-rich nanostructure, which may be related to high activity species.

Combining the results from SEM, TEM, XRD, Raman, and XPS, the novel vertically growth MoS₂ nanowalls on the SNCF is established. Such a structure could significantly increase the amount of exposed active edge sites without compromising the internal network conductivity for highly active electrocatalysis. This strategy is not only appropriate for the construction of MoS₂ nanowalls on the SNCF but also suitable for other two-dimensional nanocrystals, such as WS₂. Fig. 6 displays the successfully prepared WS₂ nanosheets on an SNCF. At the same concentration as MoS₂/SNCF, the WS₂ nanocrystals exhibit a leaf-like morphology and are uniformly grown on the surfaces of the SNCF without any aggregation. As shown in Fig. 6b, one half of the individual leaf-like WS₂ nanosheets fit closely on the SNCF substrate, and

the other half is vertically aligned on the SNCF, forming crescent-like WS₂ edges. The size of the WS₂ nanosheets ranges from 100 to 300 nm. As shown in Fig. 6a,b, most of the individual MoS₂ nanosheets exhibit the crescent-like morphology, and similarly, some adjacent WS₂ nanosheets tend to form an interleaved network. As shown in Fig. 6c, the TEM image clearly presents the interleaved WS₂ nanowalls. Fig. 6d exhibits the exposed edges of the WS₂ nanowalls, and the interlayer distance of 0.63 nm corresponds to the (002) plane of WS₂.

As shown in the HAADF-STEM image in Fig. 6e, the crescent-like WS₂ and interleaved WS₂ nanowalls both exist; however, the individual crescent-like WS₂ is dominant at this concentration of the W precursor. The STEM-EDX mapping images in Fig. 6f exhibit carbon, nitrogen, and oxygen elements, and the carbon signal corresponds with the nitrogen signal. The tungsten and sulfur signals match the crescent

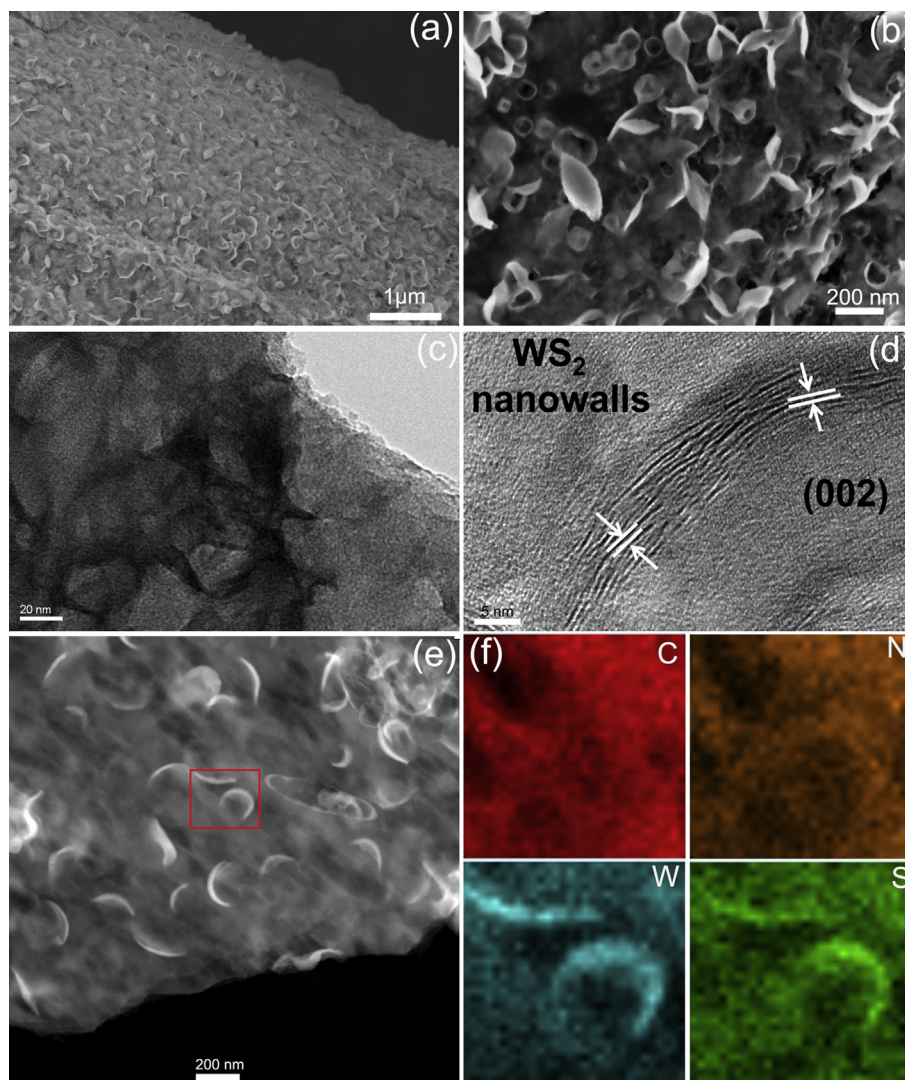


Fig. 6 – (a, b) FE-SEM, (c) TEM and (d) HRTEM images of $WS_2/SNCF$. (e) HAADF-STEM image and (f) STEM-EDS mapping images of the WS_2 nanowalls on SNCF. The concentration of W precursor was 2.2 mg mL^{-1} .

morphology well, indicating the successful preparation of the WS_2 nanosheets on N-doped CFs.

The electrocatalytic performance of the as-synthesized catalysts in acidic conditions ($0.5 \text{ M H}_2\text{SO}_4$) was evaluated using linear sweep voltammetry (LSV). Without any active processes, the HER properties of all of the samples were directly examined. Fig. 7a displays the polarization curves of the MoS_2 nanoflowers, the SNCF, the MoS_2 nanoflowers mixed with the SNCF, $WS_2/SNCF$, $MoS_2/SNCF$ and the Pt/C modified GCE. The SFs have a negligible HER activity, while the as-prepared SNCF exhibit a small HER activity. The MoS_2 exhibits an intrinsic catalytic activity toward the HER with an onset potential of -280 mV . In sharp contrast, the $MoS_2/SNCF$ with a nanowall network possesses a greatly enhanced HER activity with a smaller onset potential ($\sim -80 \text{ mV}$), accompanied by large cathodic current densities. An overpotential (η) of only 150 mV is required to achieve a current density (j) of -10 mA cm^{-2} . In addition, the $WS_2/SNCF$ with a crescent-like morphology also demonstrates good HER activity with an

onset potential of -120 mV . The commercial 20% Pt/C catalyst displays the best HER activity with a near zero onset potential.

Compared with the MoS_2 grown on the SNCF, the MoS_2 mixed with the SNCF exhibits only a weak HER activity with an onset potential of -220 mV , indicating the coupling between the SNCF and the grown MoS_2 nanowalls. The N-doped CFs not only offer a minimum diffusive resistance to mass transport at a large electrode/electrolytes interface for the charge-transfer reaction but also provide easy ion transport by shortening the diffusion pathways [42,43]. The corresponding Tafel plots of the catalysts are shown in Fig. 7b. The MoS_2 exhibits a Tafel slope of 210 mV dec^{-1} , while $WS_2/SNCF$ exhibits a lower Tafel slope of 160 mV dec^{-1} . The Tafel slope of $MoS_2/SNCF$ is approximately 70 mV dec^{-1} , indicating that the Heyrovsky mechanism is mainly responsible for the HER process. The Pt/C presents the lowest Tafel slope of 30 mV dec^{-1} , suggesting the involvement of the Tafel mechanism. The superior HER activity of the $MoS_2/SNCF$ with a nanowall network originates from the maximized exposure of

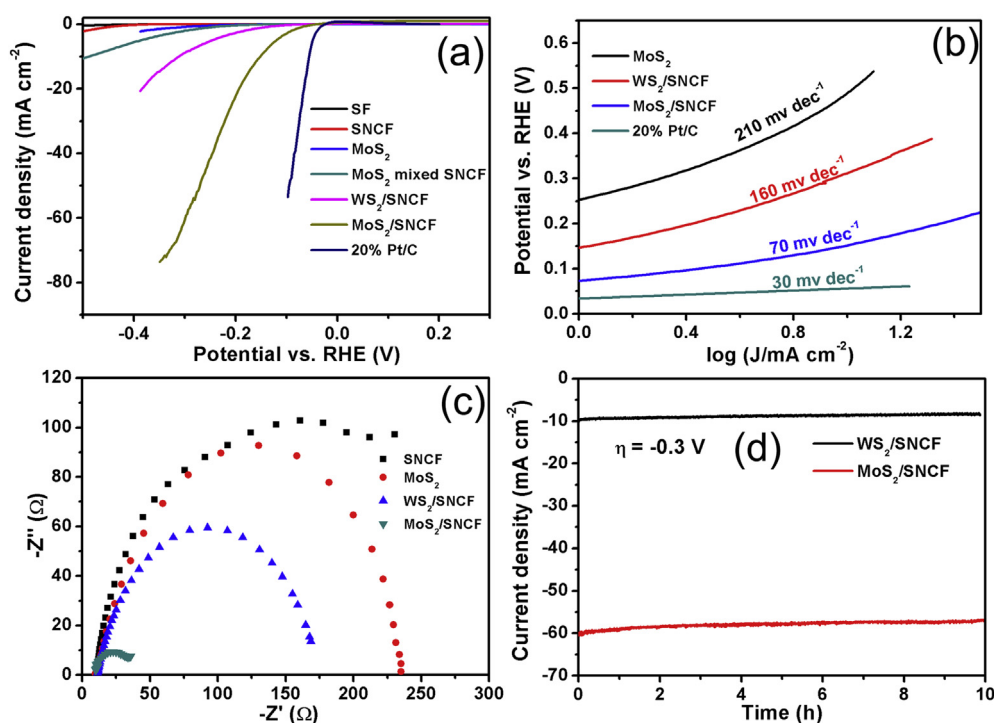


Fig. 7 – (a) Polarization curves of the SFs, MoS₂ (synthesized in DMF), the SNCF, MoS₂ mixed with the SNCF, WS₂/SNCF, MoS₂/SNCF and the Pt/C modified GCE in 0.5 M H₂SO₄ at a scan rate of 2 mV s⁻¹. (b) The Tafel plots for MoS₂ (synthesized in DMF), WS₂/SNCF, MoS₂/SNCF and the Pt/C GCE derived from their corresponding polarization curves. (c) The Nyquist plots of MoS₂ (synthesized in DMF), the SNCF, WS₂/SNCF and MoS₂/SNCF. (d) The chronoamperometric response (*j*-*t* curve) of WS₂/SNCF and MoS₂/SNCF recorded at a constant potential of 300 mV.

the active edge sites that is due to the dense and vertical growth of the MoS₂ nanosheets on the SNCF.

Apart from the high active edge exposure, an efficient electron transfer is also essential for excellent HER performance. As shown in Fig. 7c, the Nyquist plots reveal that the charge transfer resistance (R_{ct}) of MoS₂/SNCF (44.2 Ω) is much lower than that of the SNCF (321.3 Ω) and MoS₂ (238.4 Ω). The WS₂/SNCF also exhibits a lower R_{ct} of 151.7 Ω. The low value corresponds to a fast charge transfer at the interface between the electrocatalyst and the electrolyte and results in the excellent electrocatalysis for the HER. This is attributed to the synergistic effects of the N-doped carbon fibers as a highly conductive substrate to improve the conductivity of the hybrid. It is demonstrated that the MoS₂ nanowalls grown on the SNCF possess a higher conductivity and better electron transfer ability than the MoS₂ nanoflowers because of their strong electronic and chemical couplings. We further inspected the durability of MoS₂/SNCF and WS₂/SNCF, while

continuously catalyzing the HER process. As shown in Fig. 7d, at a potential of -0.3 V, the MoS₂/SNCF and WS₂/SNCF are both able to sustain continuous HER operation for 10 h under working conditions with a slight degradation in their current densities. This reveals stability under the HER conditions and suggests a strong coupling of the MoS₂ and WS₂ nanowalls with the SNCF, implying excellent durability and a prospect for practical applications (Table 1).

At the same precursor concentration, MoS₂ and WS₂ have different morphologies on the SNCF, suggesting that a variation in the concentration of the precursors may lead to various morphologies. As is well-known, the morphology of MoS₂ affects the active edge exposure directly, and there is also a structure-dependent electrocatalytic activity for the HER. Therefore, we further investigated the morphological evolutions and the related HER activity by changing the precursor concentrations of Mo and W. The concentrations of the Mo precursor were varied from 1 to 3 mg mL⁻¹. As shown in

Table 1 – Comparison of the HER parameters of several catalysts.

Catalyst	Onset η (mV)	Tafel (mv dec ⁻¹)	j at $\eta = 300$ mV vs. RHE (mA cm ⁻²)	η at $j = 10$ mA cm ⁻² (mV)
SNCF	392	350	0.6	–
MoS ₂ nanoflowers	280	210	1.1	–
MoS ₂ nanoflowers mixed with SNCF	220	190	2.2	486
WS ₂ /SNCF	120	160	9.8	310
MoS ₂ /SNCF	80	70	61.6	151
20% Pt/C	10	30	–	53

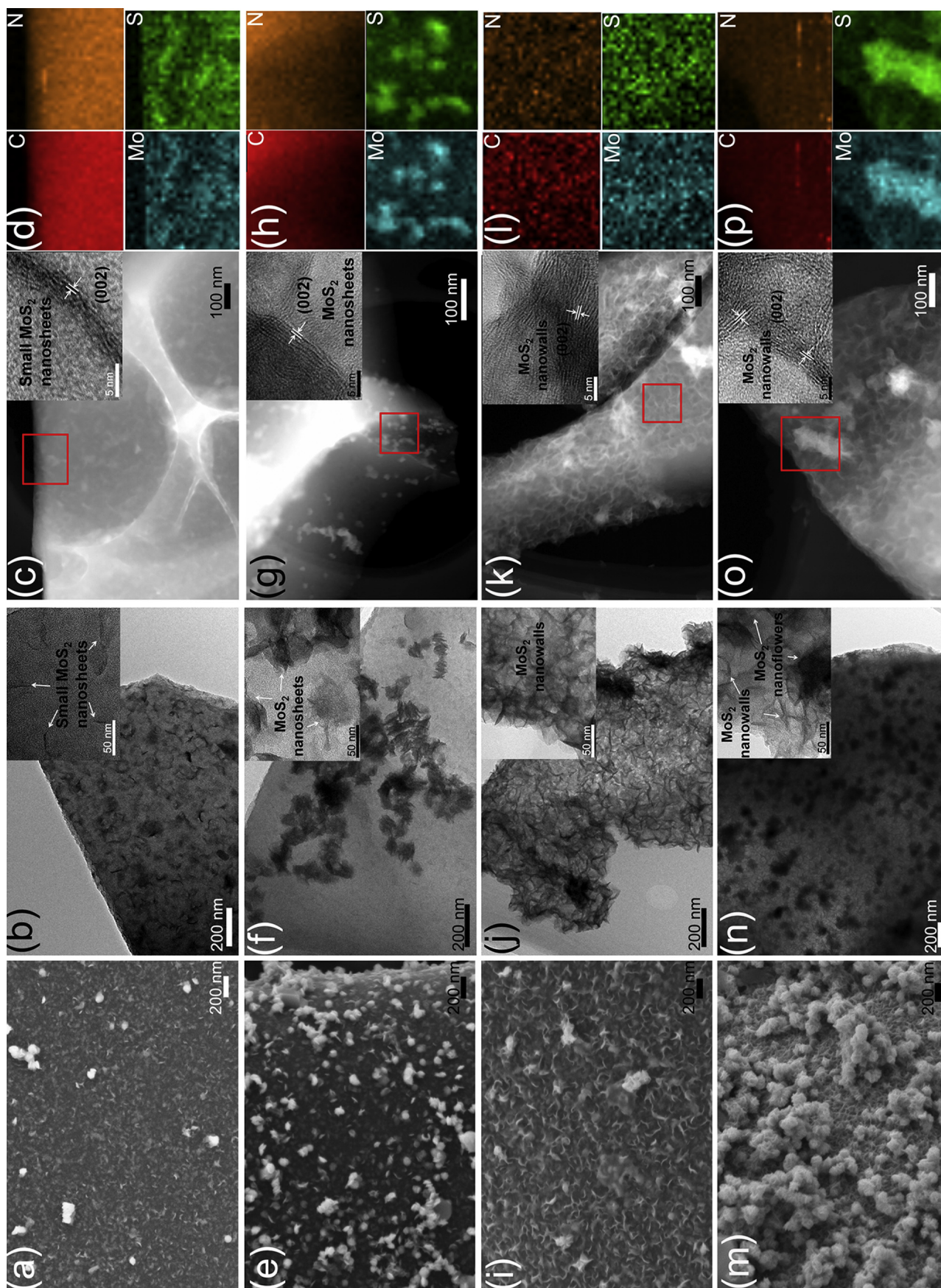


Fig. 8 – FE-SEM, TEM, HAADF-STEM and STEM-EDS mapping images of the MoS₂/SNCF hybrid prepared using different concentrations of the Mo precursor: (a–d) 1 mg mL⁻¹, (e–h) 1.5 mg mL⁻¹, (i–l) 2 mg mL⁻¹ and (m–p) 3 mg mL⁻¹.

Fig. 8a–c, at the low concentration of 1 mg mL^{-1} , a large amount of small MoS_2 nanosheets sized from 10 to 60 nm were uniformly and vertically grown on the SNCF and exhibit a crescent-like morphology. An HRTEM image of the small MoS_2 nanosheets reveals the exposed edges, and the inter-layer distance of 0.67 nm corresponds to the (002) plane of MoS_2 . STEM-EDX mapping images (Fig. 8d) also illustrate the crescent-like morphology of the small MoS_2 nanosheets.

With increased concentration (1.5 mg mL^{-1}), the as-synthesized MoS_2 nanosheets become larger (20–100 nm) and exhibit a plate-like morphology. Unlike the small vertical MoS_2 nanosheets, the larger sized MoS_2 nanoplates aggregate, as verified by Fig. 8g,h. Notably, with a higher concentration of 2 mg mL^{-1} , the whole SNCF substrate is covered with dense vertical MoS_2 nanowalls in an interleaved network, as shown in Fig. 8i–l. The size of the MoS_2 nanosheets increased to 50–200 nm. It has been reported that nucleation is mainly controlled by the solution concentration [30,31], and a high concentration would contribute to an increase in nucleation sites and the product density [31,43]. Furthermore, a lower nucleation density promotes growth at neighboring sites, which results in a slant morphology, whereas a higher nucleation density contributes to the vertical growth on the substrate because of the limited space [30,31,43]. Therefore, as the concentration increased from 1.5 to 2 mg mL^{-1} , more erect

MoS_2 nanosheets formed and led to the formation of the interleaved MoS_2 nanowalls with a high density of active edges. However, when the concentration was increased to 3 mg mL^{-1} , even though the interleaved MoS_2 nanowall networks on the SNCF formed, several aggregates of the MoS_2 nanoflowers grew on the nanowalls. They resemble rosemary buds with a number of edges buried inside in a thermodynamically stable configuration, according to the FE-SEM and TEM results (Fig. 8m–p). The poorly exposed active edges may explain the reduced HER performance.

For the synthesis of the WS_2/SNCF hybrid, a series of morphological evolutions caused by the changing of the concentration of the W precursor are shown in Fig. 9. The low concentration of 1.5 mg mL^{-1} results in sparse, slanted and well-dispersed WS_2 nanosheets, as shown in Fig. 9a,b. The small and slanted WS_2 nanosheets exhibit the crescent-like morphology, and there is no aggregation of the WS_2 nanoflowers. As shown in Fig. 9c,d, a higher concentration (2.5 mg mL^{-1}) changes the former individual crescent-like WS_2 nanosheets into the interleaved WS_2 nanowall network. Compared with 2.5 mg mL^{-1} (Fig. 10c), 3.5 mg mL^{-1} achieves vertically aligned WS_2 nanowalls with a higher density (Fig. 9e,f). The whole SNCF is covered with the WS_2 nanowall network after using a concentration of 3.5 mg mL^{-1} .

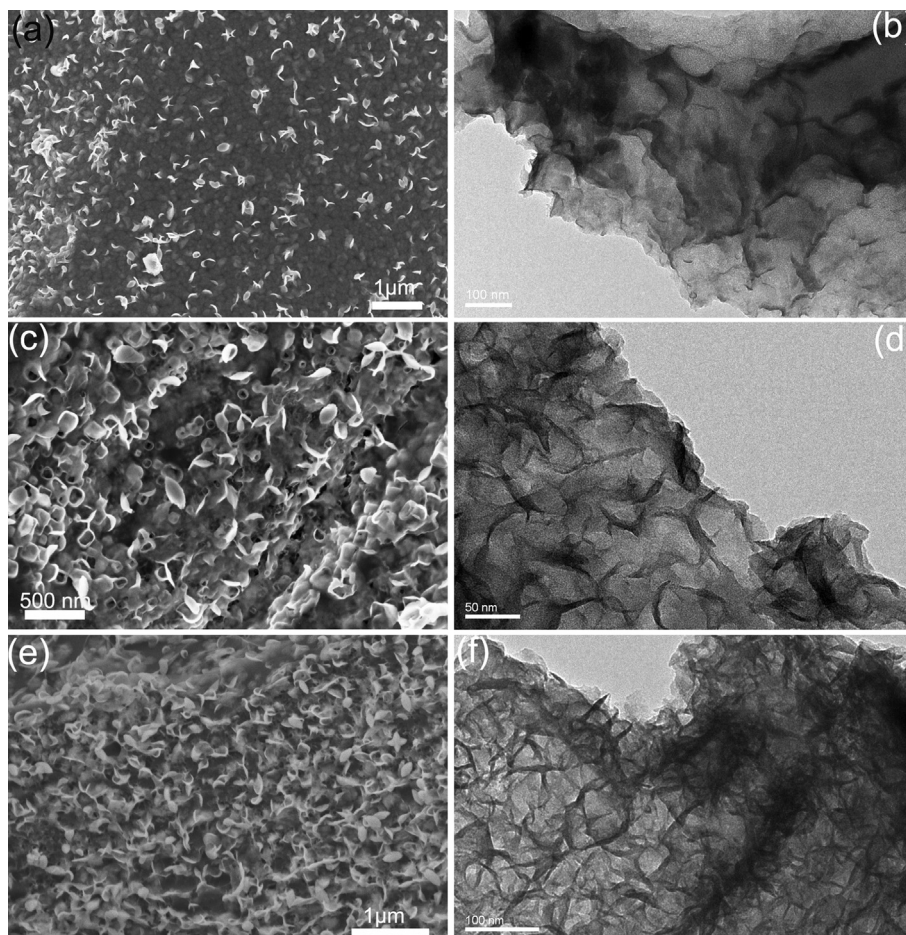


Fig. 9 – FE-SEM and TEM images of the WS_2/SNCF hybrid using different concentrations of the W precursor: (a, b) 1.5 mg mL^{-1} , (c, d) 2.5 mg mL^{-1} and (e, f) 3.5 mg mL^{-1} .

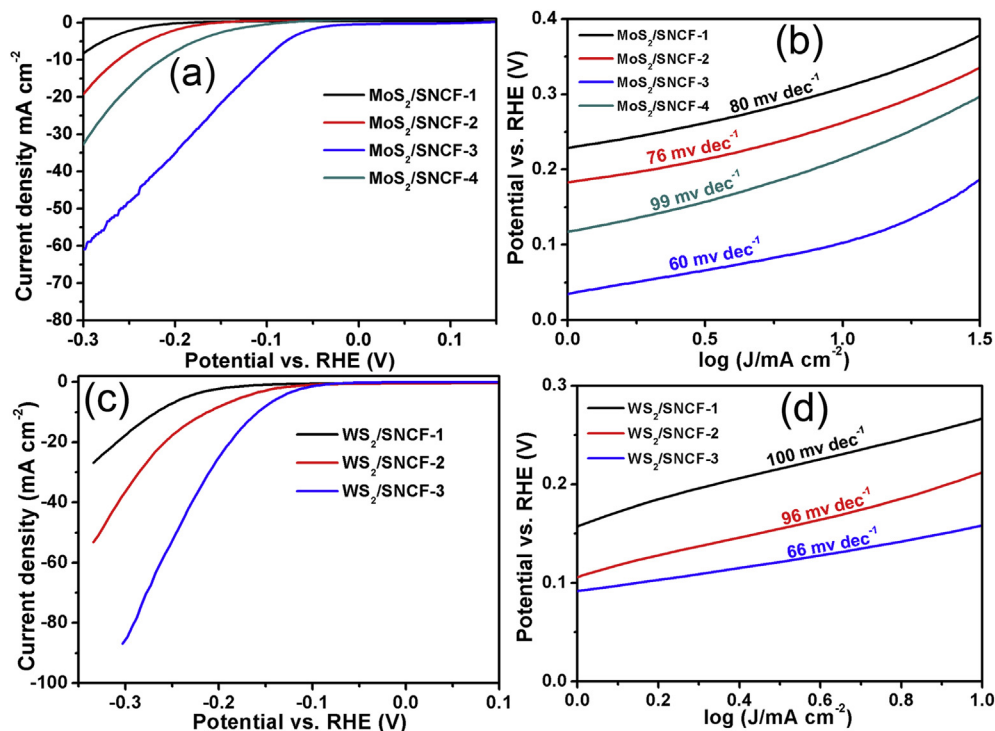


Fig. 10 – (a) Polarization curves and the corresponding (b) Tafel slopes of the MoS₂/SNCF catalysts with various morphologies in 0.5 M H₂SO₄ at a scan rate of 5 mV s⁻¹. (c) Polarization curves and the corresponding (d) Tafel slopes of the WS₂/SNCF catalysts with various morphologies in 0.5 M H₂SO₄ at a scan rate of 5 mV s⁻¹.

The corresponding electrocatalytic performances of MoS₂/SNCF and WS₂/SNCF as a function of morphology are shown in Fig. 10. The electrochemical performances of MoS₂/SNCF and WS₂/SNCF with various morphologies for the HER were demonstrated, as shown in Fig. 10. The MoS₂/SNCF catalysts prepared using concentrations of 1 mg mL⁻¹, 1.5 mg mL⁻¹, 2 mg mL⁻¹ and 3 mg mL⁻¹ are labeled as MoS₂/SNCF-1, MoS₂/SNCF-2, MoS₂/SNCF-3 and MoS₂/SNCF-4, respectively. Similarly, the WS₂/SNCF catalysts prepared using concentrations of 1.5 mg mL⁻¹, 2.5 mg mL⁻¹ and 3.5 mg mL⁻¹ are labeled as WS₂/SNCF-1, WS₂/SNCF-2 and WS₂/SNCF-3, respectively. As shown in Fig. 10a, MoS₂/SNCF-1 with individual small MoS₂ nanosheets shows a weak HER activity with an onset potential of 200 mV. An increased Mo precursor concentration (MoS₂/SNCF-3) forms the MoS₂ nanowall network and displays the best HER activity with an onset potential of 40 mV. However, compared with MoS₂/SNCF-3, MoS₂/SNCF-4 contains a larger amount of MoS₂ nanoflowers and exhibits a relatively higher

onset potential of 100 mV. The onset potentials and other criteria of the MoS₂/SNCF catalysts for the HER are shown in Table 2. The results indicate that the MoS₂/SNCF with the nanowall network exhibits the highest HER activity with the lowest onset potential and highest current density. The corresponding Tafel plots for the MoS₂/SNCF electrocatalysts present slopes of 80, 76, 60 and 99 mV dec⁻¹, as shown in Fig. 10b. The results indicate that the MoS₂/SNCF with the nanowall network possesses the lowest Tafel slope of 60 mV dec⁻¹, which proves the superior HER efficiency. Both the polarization curves and Tafel plots show the excellent HER efficiency of MoS₂/SNCF-3, which is associated with its morphology and electronic properties.

As for the electrocatalytic performance of the WS₂/SNCF series, the WS₂/SNCF with an extensive nanowall network exhibits a high HER activity with an onset potential of -96 mV (Fig. 10c; Table 2). The onset potentials of WS₂/SNCF-2 and WS₂/SNCF-1 are -134 and -201 mV, respectively, as shown in

Table 2 – Comparison of HER parameters of MoS₂/SNCF and WS₂/SNCF catalysts.

Catalyst	Onset η (mV)	Tafel (mV dec ⁻¹)	j at $\eta = 300$ mV vs. RHE (mA cm ⁻²)	η at $j = 10$ mA cm ⁻² (mV)
MoS ₂ /SNCF-1	200	80	7.9	307
MoS ₂ /SNCF-2	161	76	19.2	261
MoS ₂ /SNCF-3	40	60	60.3	102
MoS ₂ /SNCF-4	100	99	32.3	214
WS ₂ /SNCF-1	201	100	17.1	266
WS ₂ /SNCF-2	134	96	36.4	211
WS ₂ /SNCF-3	96	66	85.2	157

Fig. 10c and Table 2. The corresponding Tafel plots for the WS₂/SNCF electrocatalysts present slopes of 100, 96 and 66 mV dec⁻¹, which are superior to those of most of the WS₂-based electrocatalysts that have been previously reported. The MoS₂/SNCF and WS₂/SNCF hybrids both exhibit morphology-dependent HER activities, and the MoS₂ and WS₂ nanowall networks with large amounts of exposed active sites exhibit the best HER activities with the lowest onset potentials, lowest Tafel slopes and highest current densities [5,8,15–17,30,31,42–44].

Because of the improved effective electronic and chemical coupling between MoS₂ or WS₂ and the SNCF, electrons can be delivered directly and efficiently from the highly conductive SNCF to the vertically aligned MoS₂ nanosheets. More importantly, aligning the MoS₂ nanosheets perpendicularly to the conductive substrates optimizes the conductivity of the conductive substrates. The two-dimensional MoS₂ and WS₂ can both possess the nanowall morphology on the SNCF by adjusting the concentration of precursors. It is effective to design and construct the MoS₂ and WS₂ nanowalls with maximum active-edge exposure, leading to a high electrocatalytic activity for the HER. Based on above results, a potential growth mechanism of this outstanding MoS₂/SNCF and WS₂/SNCF is presented as follows.

The silk derived N-doped carbon fibers possess abundant oxygen groups, which can serve as anchors for the growth of MoS₂ or WS₂. At the initial stage of the reaction, the Mo and W precursors were adsorbed on the SNCF and then decomposed to form the MoS₂ or WS₂ nanosheets, which tended to nucleate and anchor on the SNCF. Because of the substrate effects, the growth of MoS₂ or WS₂ occurred in only two directions to form nanosheets. The monolayered or bilayered MoS₂ or WS₂ nanosheets were attached to each other by van der Waals interactions and finally self-assembled to form MoS₂ or WS₂ nanowall network. The appropriate and relatively high concentration of the precursor led to dense and vertically aligned nanowalls in a limited space with a large number of exposed active sites. Overall, by controlling the concentration, which can influence the nucleation and growth of MoS₂ nanosheets, the vertical growth of MoS₂ or WS₂ with a maximum exposure of active edges on the SNCF was successfully synthesized with excellent HER activities.

Conclusion

In conclusion, a facile and effective approach for the design and construction of the MoS₂ and WS₂ nanowalls with maximum active-edge exposure on silk-derived N-doped carbon fibers was demonstrated. The morphological evolutions of the MoS₂ and WS₂ nanocrystals on the SNCF, from crescent-like nanosheets to an interleaved nanowall network, can be obtained by adjusting the concentrations of the Mo and W precursors. The HER performances of the various catalysts were measured to determine the influence of the number of active edges, and a comprehensive investigation of the growth mechanisms was pursued. In the present investigation, the dense and vertically aligned MoS₂ and WS₂ nanowalls on the SNCF possessed the highest concentration of exposed active edges and exhibited outstanding HER performances. These

robust MoS₂/SNCF and WS₂/SNCF electrocatalysts exhibit preeminent HER activity with onset potentials of –40 and –96 mV and Tafel slopes of 60 and 66 mV dec⁻¹, respectively. The overpotentials (η) at $j = -10 \text{ mA cm}^{-2}$ (mV) for MoS₂/SNCF and WS₂/SNCF are –102 and –157 mV, respectively. In addition, MoS₂/SNCF and WS₂/SNCF are both able to sustain continuous HER operation for 10 h with only a slight degradation in current densities. This reveals the stability of the catalysts under HER working conditions and the strong coupling of MoS₂ and WS₂ nanowalls with the SNCF, implying excellent durability and a prospect for practical applications.

Acknowledgement

This study was supported by the National Natural Science Foundation of China (NSFC) (Grant No. 21203137, 51573166), Natural Science Foundation of Zhejiang Province (Grant No. LQ16E020005).

Appendix A. Supplementary data

Supplementary data related to this article can be found at <http://dx.doi.org/10.1016/j.ijhydene.2016.07.257>.

REFERENCES

- [1] Cabán-Acevedo M, Stone ML, Schmidt JR, Thomas JG, Ding Q, Chang HC, et al. Efficient hydrogen evolution catalysis using ternary pyrite-type cobalt phosphosulphide. *Nat Mater* 2015;14:1245–51.
- [2] Liu W, Hu E, Jiang H, Xiang Y, Weng Z, Li M, et al. A highly active and stable hydrogen evolution catalyst based on pyrite-structured cobalt phosphosulfide. *Nat Commun* 2016;7:10771–9.
- [3] Guo D, Shibuya R, Akiba C, Saji S, Kondo T, Nakamura J. Active sites of nitrogen-doped carbon materials for oxygen reduction reaction clarified using model catalysts. *Science* 2016;351:361–5.
- [4] Martínez U, Dumont JH, Holby EF, Artyushkova K, Purdy GM, Singh A, et al. Critical role of intercalated water for electrocatalytically active nitrogen-doped graphitic systems. *Sci Adv* 2016;2:e1501178.
- [5] Benck JD, Chen Z, Kuritzky LY, Forman AJ, Jaramillo TF. Amorphous molybdenum sulfide catalysts for electrochemical hydrogen production: insights into the origin of their catalytic activity. *ACS Catal* 2012;2:1916–23.
- [6] Liang Y, Li Y, Wang H, Dai H. Strongly coupled inorganic/nanocarbon hybrid materials for advanced electrocatalysis. *J Am Chem Soc* 2013;135:2013–36.
- [7] Pham KC, Chang YH, McPhail DS, Mattevi C, Andrew Wee TS, Chua DHC, et al. Amorphous molybdenum sulfide on graphene–carbon nanotube hybrids as highly active hydrogen evolution reaction catalysts. *ACS Appl Mater Interfaces* 2016;8:5961–71.
- [8] Fan X, Wang S, An Y, Lau W. Catalytic activity of MS₂ monolayer for electrochemical hydrogen evolution. *J Phys Chem C* 2016;120:1623–32.
- [9] Liu Y, Hua X, Xiao C, Zhou T, Huang P, Guo Z, et al. Heterogeneous spin states in ultrathin nanosheets induce

- subtle lattice distortion to trigger efficient hydrogen evolution. *J Am Chem Soc* 2016;138:5087–92.
- [10] Cui W, Liu Q, Xing Z, Asiri AM, Alamry KA, Sun X. MoP nanosheets supported on biomass-derived carbon flake: one-step facile preparation and application as a novel high-active electrocatalyst toward hydrogen evolution reaction. *Appl Catal B Environ* 2015;164:144–50.
- [11] Duan J, Chen S, Chambers BA, Andersson GG, Qiao SZ. 3D WS_2 nanolayers@heteroatom-doped graphene films as hydrogen evolution catalyst electrodes. *Adv Mater* 2015;27:4234–41.
- [12] Kumar K, Kim Y, Li X, Ding J, Fisher FT. Chemical vapor deposition of carbon nanotubes on monolayer graphene substrates: reduced etching via suppressed catalytic hydrogenation using C_2H_4 . *Chem Mater* 2013;25:3874–9.
- [13] Li G, Sun J, Hou W, Jiang S, Huang Y, Geng J. Three-dimensional porous carbon composites containing high sulfur nanoparticle content for high-performance lithium–sulfur batteries. *Nat Commun* 2016;7:10601–10.
- [14] Niu C, Meng J, Wang X, Han C, Yan M. General synthesis of complex nanotubes by gradient electrospinning and controlled pyrolysis. *Nat Commun* 2015;6:7402–10.
- [15] Zhu H, Zhang JF, Yanzhang RP, Du ML, Wang QF, Gao GH, et al. When cubic cobalt sulfide meets layered molybdenum disulfide: a core-shell system towards synergetic electrocatalytic water splitting. *Adv Mater* 2015;27:4752–9.
- [16] Zou ML, Chen JD, Xiao LF, Zhu H, Yang TT, Zhang M, et al. WSe_2 and $W(SexS_{1-x})_2$ nanoflakes grown on carbon nanofibers for the electrocatalytic hydrogen evolution reaction. *J Mater Chem A* 2015;3:18090–7.
- [17] Zhu H, Lyu F, Du ML, Zhang M, Wang Q, Yao JM, et al. Design of two-dimensional, ultrathin MoS_2 nanoplates fabricated within one-dimensional carbon nanofibers with thermo-sensitive morphology: high-performance electrocatalysts for the hydrogen evolution reaction. *ACS Appl Mater Interfaces* 2014;6:22126–37.
- [18] Liang Y, Wu D, Fu R. Carbon microfibers with hierarchical porous structure from electrospun fiber-like natural biopolymer. *Sci Rep* 2013;3:1119–23.
- [19] Liu J, Deng Y, Li X, Wang L. Promising nitrogen-rich porous carbons derived from one-step calcium chloride activation of biomass-based waste for high performance supercapacitors. *ACS Sustain Chem Eng* 2016;4:177–87.
- [20] Fu C, Shao Z, Fritz V. Animal silks: their structures, properties and artificial production. *Chem Commun* 2009;43:6515–29.
- [21] Murphy AR, Kaplan DL. Biomedical applications of chemically-modified silk fibroin. *J Mater Chem* 2009;19:6443–50.
- [22] Hu X, Shmelev K, Sun L, Gil ES, Park SH, Cebe P, et al. Regulation of silk material structure by temperature-controlled water vapor annealing. *Biomacromolecules* 2011;12:1686–96.
- [23] Zhang F, Zuo B, Fan Z, Xie Z, Lu Q, Zhang X, et al. Mechanisms and control of silk-based electrospinning. *Biomacromolecules* 2012;13:798–804.
- [24] Zhou L, Fu P, Cai X, Zhou S, Yuan Y. Naturally derived carbon nanofibers as sustainable electrocatalysts for microbial energy harvesting: a new application of spider silk. *Appl Catal B Environ* 2016;188:31–8.
- [25] Krywka C, Krasnov I, Figuli R, Burghammer M, Müller M. Determination of silkworm silk fibroin compressibility using high hydrostatic pressure with in situ X-ray microdiffraction. *Macromolecules* 2014;47:7187–93.
- [26] Nisal A, Trivedy K, Mohammad H, Panneri S, Gupta SS, Lele A, et al. Uptake of Azo dyes into silk glands for production of colored silk cocoons using a green feeding approach. *ACS Sustain Chem Eng* 2014;2:312–7.
- [27] Liang B, Fang L, Hu Y, Yang G, Zhu Q. Fabrication and application of flexible graphene silk composite film electrodes decorated with spiky Pt nanospheres. *Nanoscale* 2014;6:4264–74.
- [28] Wang HY, Zhang YQ. Effect of regeneration of liquid silk fibroin on its structure and characterization. *Soft Matter* 2013;9:138–45.
- [29] Wei X, Wan S, Jiang X, Wang Z, Gao S. Peanut-shell-like porous carbon from nitrogen-containing poly-N-phenylethanolamine for high-performance supercapacitor. *ACS Appl Mater Interfaces* 2015;7:22238–45.
- [30] Zhang N, Gan S, Wu T, Ma W, Han D, Niu L. Growth control of MoS_2 nanosheets on carbon cloth for maximum active edges exposed: an excellent hydrogen evolution 3D cathode. *ACS Appl Mater Interfaces* 2015;7:12193–202.
- [31] Sen UK, Mitra S. High-rate and high-energy-density lithium-ion battery anode containing 2D MoS_2 nanowall and cellulose binder. *ACS Appl Mater Interfaces* 2013;5:1240–7.
- [32] Zhang C, Fu L, Liu N, Liu M, Wang Y, Liu ZF. Synthesis of nitrogen-doped graphene using embedded carbon and nitrogen sources. *Adv Mater* 2011;23:1020–4.
- [33] Huang X, Zou X, Meng Y, Mikmekova E, Chen H. Yeast cells-derived hollow core/shell heteroatom-doped carbon microparticles for sustainable electrocatalysis. *ACS Appl Mater Interfaces* 2015;7:1978–86.
- [34] Koroteev VO, Bulusheva LG, Asanov IP, Shlyakhova EV, Vyalikh DV, Okotrub AV. Charge transfer in the MoS_2 /carbon nanotube composite. *J Phys Chem C* 2011;115:21199–204.
- [35] Hou J, Cao C, Idrees F, Ma X. Hierarchical porous nitrogen-doped carbon nanosheets derived from silk for ultrahigh-capacity battery anodes and supercapacitors. *ACS Nano* 2015;9:2556–64.
- [36] Jiang T, Wang Y, Wang K, Liang Y, Wu D. A novel sulfur-nitrogen dual doped ordered mesoporous carbon electrocatalyst for efficient oxygen reduction reaction. *Appl Catal B Environ* 2016;189:1–11.
- [37] Shen W, Fan W. Nitrogen-containing porous carbons: synthesis and application. *J Mater Chem A* 2013;1:999–1013.
- [38] Chen Y, Liu Q, Wang J. Carbon dioxide activated carbon nanofibers with hierarchical micro-/mesoporosity towards electrocatalytic oxygen reduction. *J Mater Chem A* 2016;4:5553–60.
- [39] Li P, Xing C, Qu S, Li B, Shen W. Carbon dioxide capturing by nitrogen-doping microporous carbon. *ACS Sustain Chem Eng* 2015;3:1434–42.
- [40] Liu W, Chen Z, Zhou G, Sun Y, Lee HR, Liu C, et al. 3D porous sponge-inspired electrode for stretchable lithium-ion batteries. *Adv Mater* 2016;28:3578–83.
- [41] Wang T, Zhuo J, Du K, Chen B, Zhu Z, Shao Y, et al. Electrochemically fabricated polypyrrole and MoS_x copolymer films as a highly active hydrogen evolution electrocatalyst. *Adv Mater* 2014;26:3761–6.
- [42] Zhu H, Du ML, Zhang M, Zou ML, Yang TT, Wang SL, et al. S-rich single-layered MoS_2 nanoplates embedded in N-doped carbon nanofibers: efficient co-electrocatalysts for the hydrogen evolution reaction. *Chem Commun* 2014;50:15435–8.
- [43] Zheng X, Xu J, Yan K, Wang H, Wang Z, Yang S. Space-confined growth of MoS_2 nanosheets within graphite: the layered hybrid of MoS_2 and graphene as an active catalyst for hydrogen evolution reaction. *Chem Mater* 2014;26:2344–53.
- [44] Kibsgaard J, Chen Z, Reinecke BN, Jaramillo TF. Engineering the surface structure of MoS_2 to preferentially expose active edge sites for electrocatalysis. *Nat Mater* 2012;11:963–9.